Volume 23
Number 21
7 June 2021
Pages 3763–3930

CrystEngComm

rsc.li/crystengcomm

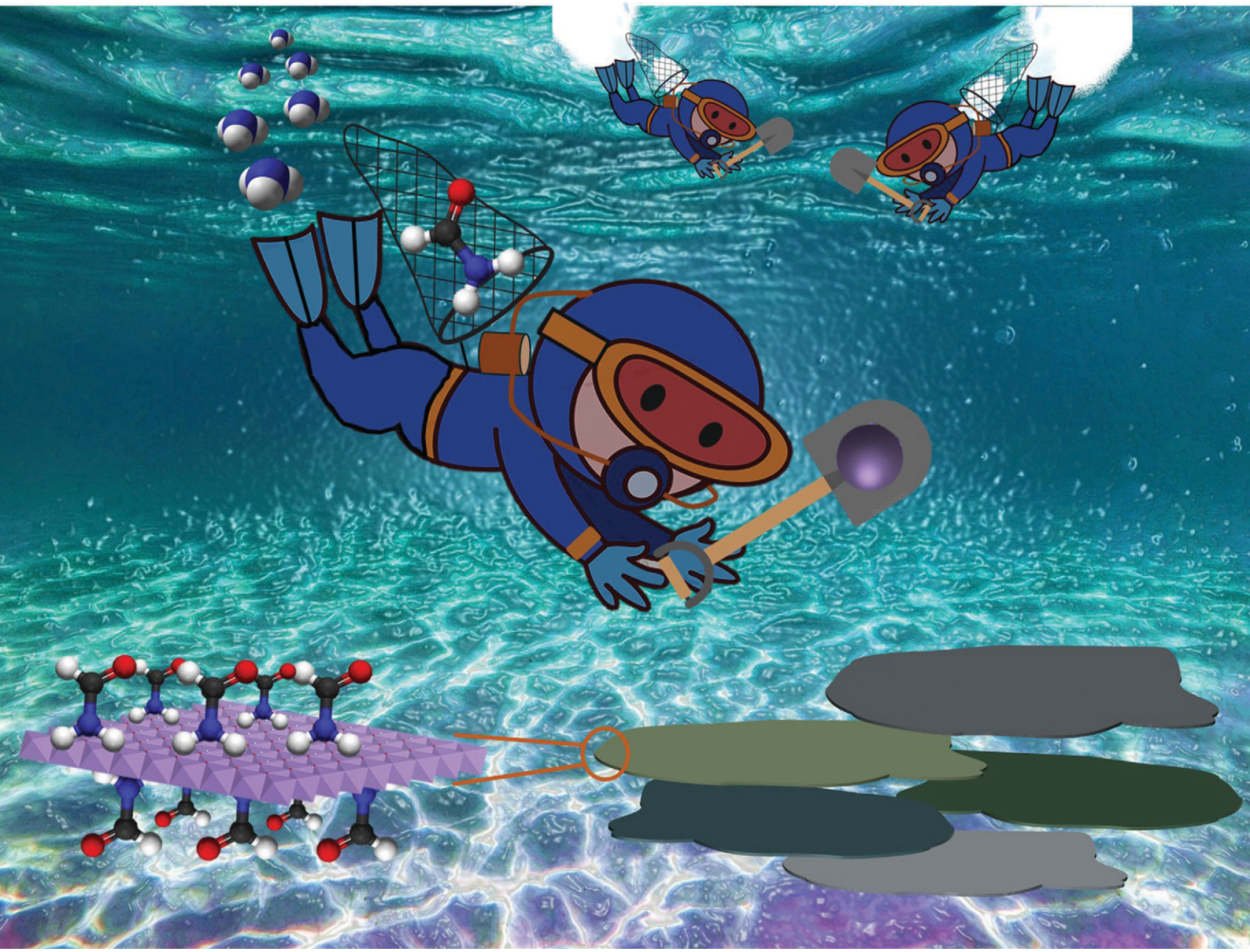

ISSN 1466-8033

ROYAL SOCIETY OF CHEMISTRY

PAPER
Minghua Huang, Helmut Cölfen *et al.*
Synthesis of ultrathin metal oxide and hydroxide nanosheets using formamide in water at room temperature

CrystEngComm

ROYAL SOCIETY OF CHEMISTRY

PAPER

View Article Online
View Journal | View Issue

Cite this: *CrystEngComm*, 2021, **23**, 3794

Synthesis of ultrathin metal oxide and hydroxide nanosheets using formamide in water at room temperature†

Zongkun Chen,[a] Minghua Huang *[b] and Helmut Cölfen *[a]

Received 25th February 2021,
Accepted 24th April 2021

DOI: 10.1039/d1ce00277e

rsc.li/crystengcomm

The rational preparation of ultrathin two-dimensional metal oxide and hydroxide nanosheets is the first and crucial step towards their utilization in both fundamental research and practical applications. From the perspective of the production cost, the further development of such materials remains a challenging task. Therefore, it is highly desirable to synthesize these materials *via* a simple and general strategy at room temperature. Besides, less attention has been paid to investigate their growth process, leading to ambiguous formation mechanisms and the lack of guiding principles for designing the targeted ultrathin 2D metal oxides and hydroxides. Here, 6 different ultrathin (<5 nm) 2D metal oxides and hydroxides have been successfully synthesized *via* a simple precipitation route in formamide aqueous solution at room temperature. Detailed investigations demonstrate that the formation of the ultrathin morphology relies on the inhibition of the *z*-direction growth by the $-NH_2$ groups of the formamide molecules. These findings broaden the fundamental understanding of 2D material formation mechanisms and inspire interest in extending this strategy to further systems. Our study opens a new avenue for an easy, general and room temperature synthesis of ultrathin 2D metal oxides and hydroxides.

Introduction

Ultrathin two-dimensional (2D) nanomaterials, such as metal oxides,[1–4] metal hydroxides,[5–7] metal chalcogenides,[8,9] metal carbides[10,11] and black phosphorus,[12,13] have been and continue to be of great interest to researchers since the experimental discovery of graphene.[14,15] In particular, attractive advantages of ultrathin 2D metal oxides and hydroxides set them apart from other materials owing to their wide structural and chemical variety, broad applications, potential low-cost mass production and shape-preserving transformation into other materials. Because the rational preparation of ultrathin 2D metal oxides and hydroxides represents the first and crucial step towards their utilization in both fundamental research and practical applications, considerable research efforts have been made in the past decade to develop a facile and scalable synthesis strategy. Although exfoliation of bulk layered materials into single- or few-layer nanosheets is regarded as one of the most promising synthesis strategies, such a top-down strategy comes inevitably with several inherent drawbacks such as relatively low yields, time-consuming steps, difficulty in scaling up and complicated multi-step operations. The recent rational trend to directly synthesize ultrathin 2D metal oxides and hydroxides *via* a bottom-up approach, especially *via* a wet-chemical bottom-up route, is attracting rising interest,[16,17] as a result of the advantages of this route associated with its time-saving, scalable, efficient and easy synthesis process. Accordingly, various methods belonging to this route, including pulsed-laser ablation,[18] one-step direct synthesis in the presence of special additives (sodium dodecyl sulfate, hydrophobic ionic liquid, formamide, *etc.*),[19–21] hydrothermal synthesis using a high concentration of H_2O_2 as the solvent,[22] a microwave-assisted liquid phase method,[23] green synthesis of 2D nanomaterials at room temperature using liquid metal reaction media,[24,25] electrochemical deposition on certain substrates,[26] *etc.*, have been explored. Note that one-step direct synthesis methods in the presence of special additives stand out from the competition with other wet-chemical bottom-up methods benefiting from their potential in avoiding the drawbacks of utilizing special facilities/reactants and the energy consumption *via* elevated reaction temperature during the synthesis process. This is in favor of realizing the low-cost and large-scale synthesis of ultrathin 2D metal oxides and hydroxides. Among different additives, formamide is the most commonly used one.[17,20,27] Unfortunately, current synthesis strategies involving

[a] *Physical Chemistry, University of Konstanz, Universitätsstraße 10, D-78457 Konstanz, Germany. E-mail: helmut.coelfen@uni-konstanz.de*
[b] *School of Materials Science and Engineering, Ocean University of China, 266100 Qingdao, China. E-mail: huangminghua@ouc.edu.cn*

† Electronic supplementary information (ESI) available. See DOI: 10.1039/d1ce00277e

formamide vary from one system to the other and preparing various target materials still remains challenging by using one and the same facile strategy at room temperature,[20] significantly impeding the general fabrication and the further development of relevant materials. Besides, progress in the preparation and application of corresponding ultrathin nanomaterials has not been paralleled by a concomitant development of their formation mechanism. More specifically, although previous studies proposed that the successful formation of ultrathin nanosheets results from the unusually high dielectric constant of formamide and interactions between the carbonyl groups of formamide and the hydroxyl layers on the hydroxide sheet surfaces,[20] the exact function of formamide on forming the ultrathin structure has not been fully demonstrated, which is detrimental to the rational design and preparation of the desirable target material. Summing up the above analysis, both fabricating ultrathin 2D metal oxides and hydroxides in the presence of formamide *via* an improved synthesis strategy and investigating the formation mechanism of such materials are lucrative.

Herein, we describe a simple and general wet-chemical precipitation strategy, which involves the reaction between metal ions and OH^- produced by the NH_3-initiated protonation process, to produce hydroxide nanomaterials in formamide aqueous solution at room temperature. Different types of ultrathin 2D metal oxide and hydroxide nanosheets, namely $Co_3O_4/Co(OH)_2$, γ-Fe_2O_3, Mn_3O_4, ZnO, $Cu(OH)_2{\cdot}H_2O$ and $Mg(OH)_2/Mg_2(OH)_3Cl$, with a thickness of less than 5 nm can be successfully synthesized under the same conditions except for changing the original metal salt. Note that obtaining a metal oxide phase instead of a metal hydroxide phase using the several systems is ascribed to the crystal phase change from hydroxide to oxide, which is caused by the topological transformation during the reaction process. Detailed investigations were carried out to study the formation mechanism of these ultrathin nanomaterials using Fourier transform infrared spectroscopy (FTIR) and nuclear magnetic resonance (NMR) spectroscopy. The obtained results reveal that, except for the unusually high dielectric constant of formamide and interactions between the carbonyl groups of formamide and the hydroxyl layers, the $-NH_2$ groups of formamide also play a key role in decreasing the thickness of the nanosheets. To the best of our knowledge, this is the first work clarifying the effect of $-NH_2$ groups on inhibiting the growth of nanosheets along the *z*-direction, providing important insights into guiding the synthesis of the desired ultrathin 2D metal oxides and hydroxides. Since the growth mechanism depends mainly on the layered structure character of the target materials instead of the individual character of metal elements, we believe that this strategy can be extended to a vast number of other systems, offering new opportunities for an easy, general, low-cost and room temperature synthesis of ultrathin 2D metal oxide and hydroxide nanosheets.

Experimental

Materials

Ammonium hydroxide solution (28–30 wt% solution of NH_3 in water) was obtained from Acros Organics (Geel, Belgium). $FeCl_2{\cdot}4H_2O$ was bought from Alfa Aesar. $MgCl_2{\cdot}6H_2O$ and $Cu(CH_3COO)_2{\cdot}H_2O$ were obtained from Fluka. Other reagents were purchased from Sigma-Aldrich. All chemicals were of analytical grade and were used as received without any further purification. Water used for the preparation of aqueous solutions was purified using a Millipore-Q water purification system.

Synthesis of nanosheets

A typical procedure is described as follows: a solution containing precursor (*X* mM) was prepared by dissolving the metal salts in a mixed solution of water (*Y* mL) and solvent B (*Z* mL). After ultrasonic dissolution, the vial was then sealed with Parafilm and three pinholes were drilled allowing for gas diffusion. Subsequently, the vial was put into a sealed blue cap bottle (100 mL) with 2 mL of concentrated ammonium hydroxide solution. After the diffusion for 12 hours at room temperature, the precipitate found at the bottom of the vial was washed two times by centrifugation (9000 rpm, 5 min) with Milli-Q water and dried at room temperature. More details about the synthesis protocol are provided in the ESI.†

Characterization

Transmission electron microscopy (TEM) images and selected area electron diffraction (SAED) patterns were acquired on a Zeiss Libra 120 microscope operating at 120 kV. The TEM samples were prepared from ethanol dispersion or water solution on conventional TEM grids (carbon-coated copper grids, 400 mesh, supplied by Quantifoil GmbH). X-ray powder diffraction (XRD) data were acquired on a D8 ADVANCE and DAVINCI.DESIGN (Bruker) X'pert diffractometer with Cu Kα radiation. Scanning electron microscopy (SEM) was conducted using a Zeiss CrossBeam 1540XB reaching a resolution of up to 1.1 nm at 20 kV and the acceleration voltage can be changed from 0.1 to 30 kV. It was equipped with an SE2 and an InLens detector. Attenuated-total-reflection-infrared spectroscopy (ATR-FTIR) was conducted on a Vertex 80 V spectrometer (Bruker Optics). The thickness of the nanomaterials was characterized with a JPK NanoWizard atomic force microscope (AFM) in the intermittent contact mode using a silicon tip. X-ray photoelectron spectra (XPS) were obtained on a Thermo ESCALAB 250XI with Mg Kα radiation ($h\upsilon$ = 1253.6 eV) as the excitation source. High-resolution TEM (HRTEM) images were obtained on a JEOL-2010 microscope operated at 200 kV. The titration setup is a commercial, computer-controlled titration system manufactured by Metrohm. The titration software is Tiamo 2.2. Solution phase ^{13}C NMR spectra were recorded using a Bruker Avance III 400 operating at 400

MHz. Sample preparation procedures for the measurement of solution phase ^{13}C NMR spectrum can be found in the ESI.† The 3D crystal structures below were extracted from the ICSD database using Materials Studio 5.5 (Accelrys) and displayed after improvements to the number of units.

Results and discussion

As illustrated in Scheme 1, the synthesis strategy used mainly involves the diffusion of ammonia vapor (NH_3) originating from ammonium hydroxide into formamide aqueous solution containing metal ion salts, triggering a reaction between the NH_3 molecule and water molecule of the reaction solution to generate OH^-, namely $NH_3 + H_2O \rightleftharpoons NH_4^+ + OH^-$, which could increase the pH value of the solution. The increased pH enables the hydrolysis of metal ions to initiate the precipitation of metal hydroxides. In this strategy, formamide molecules play a key role in influencing the thickness of the final hydroxide product. Note that by simply changing the type of the metal salt precursors, six different ultrathin 2D nanosheets could be successfully synthesized using the same protocol. The crystallinity of these nanosheet products was studied by powder XRD. As displayed in Fig. 1, the XRD patterns of the different nanosheet products can be well-indexed to $Co_3O_4/Co(OH)_2$, γ-Fe_2O_3, Mn_3O_4, ZnO, $Cu(OH)_2{\cdot}H_2O$ and $Mg(OH)_2/Mg_2(OH)_3Cl$ phases, respectively, suggesting the successful formation of the corresponding metal oxides or hydroxides in the different systems. The diffraction peaks of the various nanosheet products were sharp and intense, indicating their high crystallinity, which might benefit from the slow reaction process caused by the gas-diffusion strategy. Note that the generation of metal oxides, namely Co_3O_4, γ-Fe_2O_3, Mn_3O_4 and ZnO, is ascribed to the crystal phase change from hydroxide to oxide caused by the topological transformation during the reaction process, which has been well documented by previous studies.[28–31] XPS was employed to evaluate the surface composition and electronic states of these metal oxide and hydroxide nanosheets. The survey spectra provided in Fig. S1† indicate the existence of O and corresponding metal elements for these six ultrathin 2D nanosheets, which agrees well with the composition of the aforementioned metal oxide and hydroxide nanosheets. The high-resolution XPS spectra of these metal elements are shown in Fig. 2 to analyze their electronic states. As presented in Fig. 2A, the high-resolution XPS spectrum of Co 2p comprises two spin–orbital peaks together with two satellite peaks. The Co 2p1/2 peak can be deconvoluted into two sub-peaks centering at 796.4 and 795 eV, and the Co 2p3/2 peak can be deconvoluted into two sub-peaks centering at 781 and 780 eV. The binding energies at 780 and 795 eV agree well with the signal of Co^{3+}, while the other two peaks at 781 and 796.4 eV correspond to the signal of Co^{2+},[32] suggesting the coexistence of Co^{2+} and Co^{3+}, which is consistent with the presence of the Co_3O_4 and $Co(OH)_2$ phases suggested by the XRD results. Similarly, two pairs of doublets in the deconvolution results of the Mn 2p spectrum (Fig. 2C) reveal two kinds of electronic states (Mn^{2+} and Mn^{3+}) existing in the Mn_3O_4 nanosheets,[33] supporting the successful formation of the Mn_3O_4 phase. Besides, the other high-resolution XPS spectra of Fe 2p for γ-Fe_2O_3, Zn 2p for ZnO, Cu 2p for $Cu(OH)_2{\cdot}H_2O$ and Mg 1s for $Mg(OH)_2/Mg_2(OH)_3Cl$ nanosheets confirm the existence of the corresponding electronic states, namely Fe^{3+}, Zn^{2+}, Cu^{2+} and Mg^{2+},[34–39] which is in line with the aforesaid XRD results.

The morphology of these six 2D materials was investigated by conducting SEM and TEM. As shown in Fig. 3A–F, all of them show 2D nanosheet morphologies, but with different sizes. To be more specific, the Mn_3O_4, ZnO, and $Mg(OH)_2/Mg_2(OH)_3Cl$ nanosheets possess a lateral size of about several μm, while the $Co_3O_4/Co(OH)_2$, γ-Fe_2O_3 and $Cu(OH)_2{\cdot}H_2O$ nanosheets are several hundred nanometers in lateral size. The planar 2D morphology can be further verified by the TEM results (Fig. 3G–L). In the TEM images, the high transparency and the flexible feature represent indirect proof of the ultrathin thickness of these nanosheets. To determine the exact thickness, AFM was utilized and the results indicate that most of the 2D metal oxide and hydroxide nanosheets have a thickness of 3 ± 2 nm (Fig. S2†), manifesting the formation of the ultrathin structure. Further characterization was performed using SAED and HRTEM to evaluate the crystallinity of the 2D nanosheets. In the SAED patterns, the well-ordered bright spots of the various nanosheets (Fig. 3M–R) reveal their high-quality single-crystalline nature, with the exception of the typical ring-pattern of $Cu(OH)_2{\cdot}H_2O$ that demonstrates its polycrystallinity. Besides, the SAED patterns taken from the plane region of the nanosheets can be indexed to the diffraction patterns of the [001] zone axis for $Co_3O_4/Co(OH)_2$, [111] zone axis for γ-Fe_2O_3, [010] zone axis for Mn_3O_4, [001] zone axis for ZnO and [001] zone axis for $Mg(OH)_2/Mg_2(OH)_3Cl$, confirming that the $Co_3O_4/Co(OH)_2$, γ-Fe_2O_3, Mn_3O_4, ZnO and $Mg(OH)_2/Mg_2(OH)_3Cl$ nanosheets are respectively exposed with the {001}, {111}, {010}, {0001} and {001} crystal planes. The HRTEM images of the corresponding 2D nanosheets (Fig. 3S–X) show clear lattice fringes with the lattice spacings of 0.23 nm, 0.296 nm, 0.29 nm, 0.28 nm, 0.26 nm and 0.27 nm, matching well with the (101) plane of $Co(OH)_2$, (220) plane of γ-Fe_2O_3, (200) plane of Mn_3O_4, (100) plane of ZnO, (120) plane of $Cu(OH)_2{\cdot}H_2O$ and

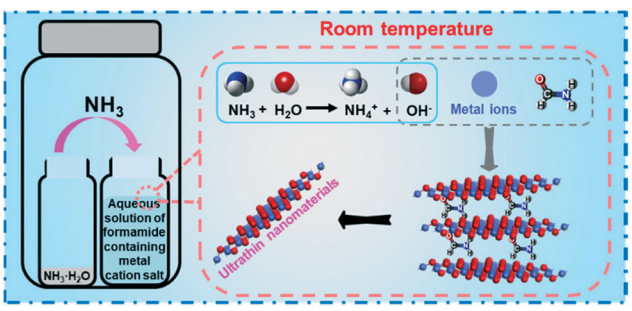

Scheme 1 A schematic illustration of the synthesis strategy for the ultrathin two-dimensional metal oxide and hydroxide nanosheets.

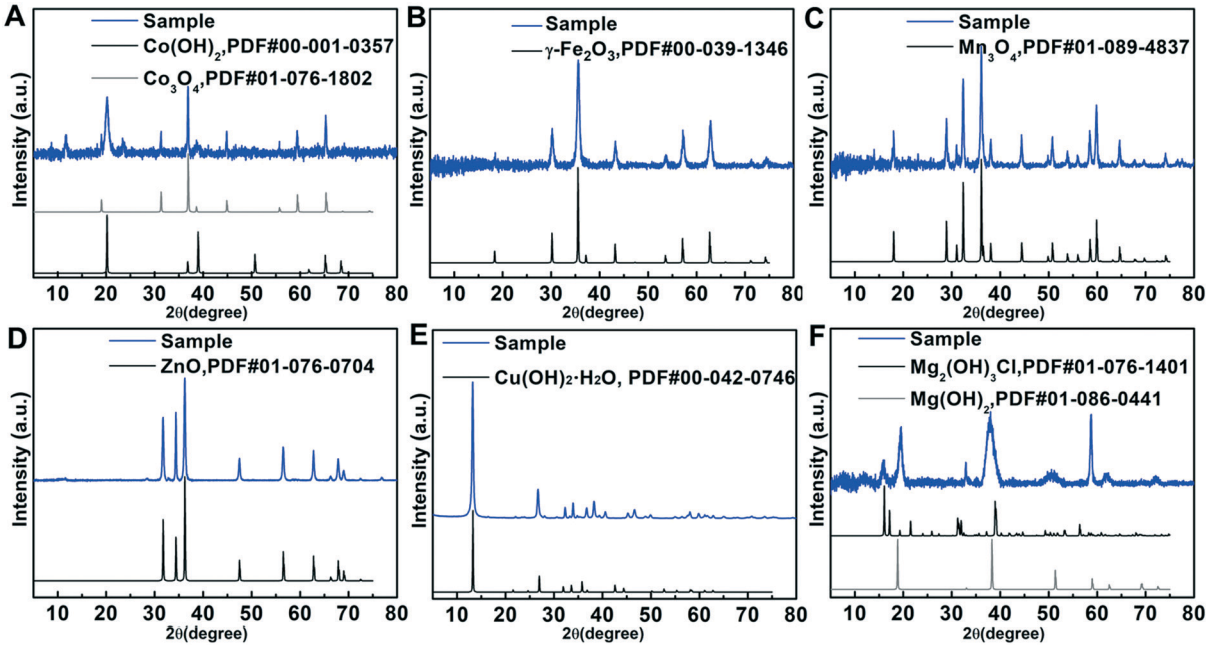

Fig. 1 XRD patterns of the ultrathin two-dimensional metal oxide and hydroxide nanosheets: (A) $Co_3O_4/Co(OH)_2$, (B) γ-Fe_2O_3, (C) Mn_3O_4, (D) ZnO, (E) $Cu(OH)_2{\cdot}H_2O$ and (F) $Mg(OH)_2/Mg_2(OH)_3Cl$.

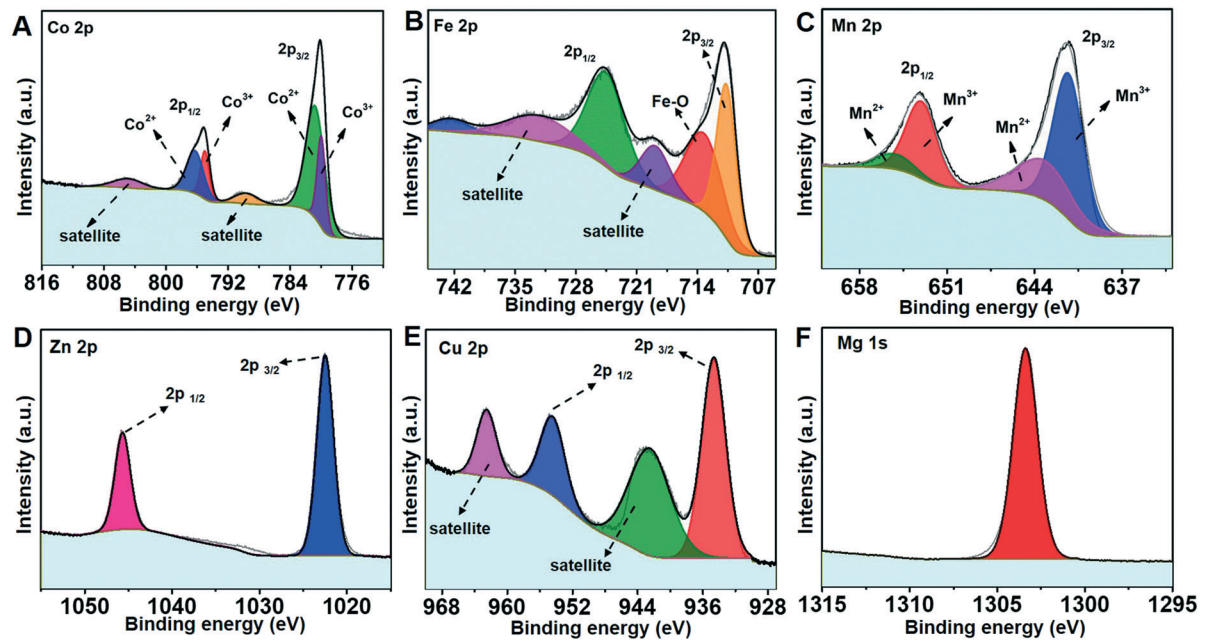

Fig. 2 (A) XPS Co 2p spectrum of $Co_3O_4/Co(OH)_2$, (B) XPS Fe 2p spectrum of γ-Fe_2O_3, (C) XPS Mn 2p spectrum of Mn_3O_4, (D) XPS Zn 2p spectrum of ZnO, (E) XPS Cu 2p spectrum of $Cu(OH)_2{\cdot}H_2O$ and (F) XPS Mg 1s spectrum of $Mg(OH)_2/Mg_2(OH)_3Cl$.

(100) plane of $Mg(OH)_2$, respectively, which further confirmed the high crystallinity and the exposed faces of these nanosheets.

To establish the guiding synthesis principles for other ultrathin nanosheets, it is necessary to fully understand the factors that determine the formation of the here obtained six ultrathin nanosheets. Reference experiments were conducted using the same synthesis protocol but without the addition of formamide to verify the influence of formamide on the formation of ultrathin nanosheets. The SEM images provided in Fig. S3† show the 2D morphology of the obtained reference products, suggesting their preferential growth habit along one layer during the growth process, which can be explained by the preferential growth along one layer for materials with a layered structure under suitable experimental conditions.[23] It is known that $Co(OH)_2$,

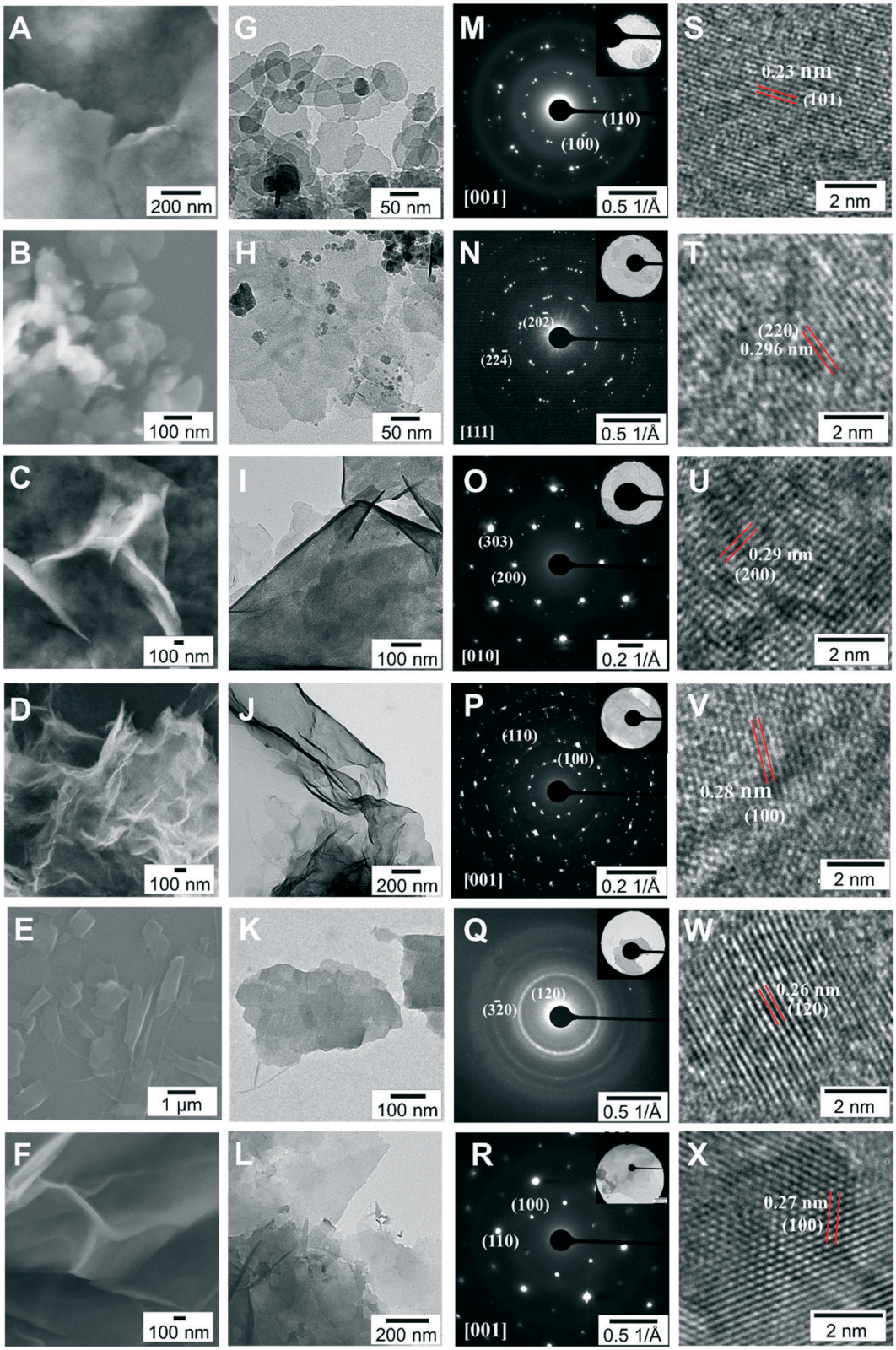

Fig. 3 SEM images, TEM images, SAED patterns and HRTEM images of the 2D nanomaterials: (A, G, M and S) $Co_3O_4/Co(OH)_2$, (B, H, N and T) γ-Fe_2O_3, (C, I, O and U) Mn_3O_4, (D, J, P and V) ZnO, (E, K, Q and W) $Cu(OH)_2{\cdot}H_2O$, and (F, L, R and X) $Mg(OH)_2/Mg_2(OH)_3Cl$.

$Fe(OH)_2$, $Mn(OH)_2$, $Zn(OH)_2$, $Cu(OH)_2{\cdot}H_2O$ and $Mg(OH)_2$ have typical layered structures with strong in-plane chemical bonding and weak van der Waals forces between different layers (Fig. 4A), and thus the preferential growth along one

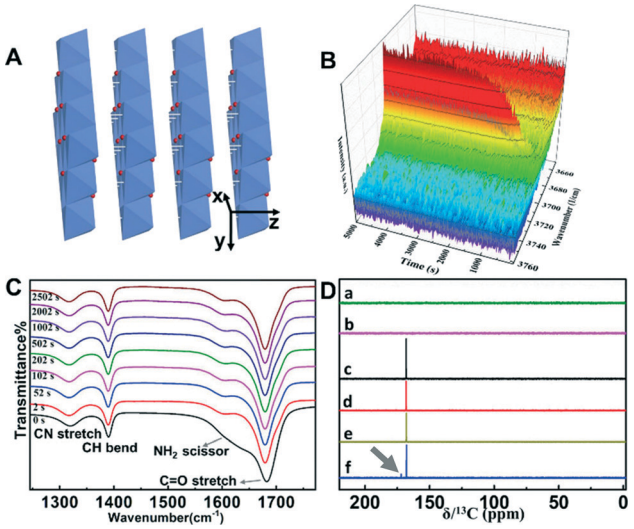

Fig. 4 (A) Atomic structure of $Co(OH)_2$, $Fe(OH)_2$, $Mn(OH)_2$, $Zn(OH)_2$, $Cu(OH)_2{\cdot}H_2O$ and $Mg(OH)_2$. (B) Evolution of the typical O–H stretching mode of the Mg–OH groups over time. (C) FTIR spectra of the reaction process after introducing NH_3 into the formamide aqueous solution containing $MgCl_2$ in the 1000–2000 cm^{-1} region. (D) ^{13}C NMR spectra of (a) pure water after introducing NH_3, (b) aqueous solution containing $MgCl_2$ after introducing NH_3, (c) pure formamide aqueous solution, (d) formamide aqueous solution containing $MgCl_2$, (e) formamide aqueous solution after introducing NH_3 without $MgCl_2$ and (f) formamide aqueous solution containing $MgCl_2$ after introducing NH_3.

layer could be easily realized. Note that compared to these obtained reference products, we found that the nanomaterials synthesized in formamide aqueous solution show thinner structures, implying that formamide molecules have a positive effect on decreasing the thickness of the nanosheets. To understand the driving force originating from formamide for inhibiting the growth of nanosheets along the *z*-direction, taking the $Mg(OH)_2/Mg_2(OH)_3Cl$ system as an example, additional reference experiments were performed using the same protocol but with the replacement of formamide by other organic solvents or additives possessing various functional groups, structures, dielectric constants, *etc.* Fig. S4† presents the molecular formula of the organic solvents or additives used and the morphology of the corresponding final products as observed by SEM. It can be seen that nanomaterials synthesized in the reaction solutions containing dimethylformamide or ethanol tend to grow thicker, demonstrating that dimethylformamide or ethanol might have no influence over inhibiting the *z*-direction growth. In contrast, ultrathin nanosheets could be obtained when formamide was replaced with one of the following organic solvents or additives: ethanolamine, ethylenediamine, glycine and hydrazine. Note that ethanolamine has a low dielectric constant (Table S1†) and carbonyl groups are absent in hydrazine, ethanolamine and ethylenediamine, which calls into question that the formation of ultrathin structures is related to the unusually high dielectric constant of organic solvents and interactions between the carbonyl groups of organic solvents and the hydroxyl layers on the hydroxide sheet surfaces.[20] More importantly, based on the fact that ultrathin nanosheets could form when hydrazine (NH_2–NH_2) was used as the organic solvent (Fig. S4A†), it is reasonable to infer that, except for the aforesaid two factors, the –NH_2 groups also play a key role in the inhibition of the *z*-direction growth.

FTIR was utilized to verify the interaction between the –NH_2 groups and the formed hydroxide *via* monitoring the signal change of the functional groups during the reaction process. Note that we monitored the reaction process of one-off addition of 2 mL of concentrated $NH_3{\cdot}H_2O$ into the reaction solution, because it is difficult to *in situ* monitor the reaction process of NH_3-diffusion into the reaction solution. As shown in Fig. S5,† the one-off addition of 2 mL of concentrated $NH_3{\cdot}H_2O$ into the reaction solution leads to the formation of nanosheets with a similar morphology to that of the NH_3-diffusion method, indicating that the former is a suitable alternative to investigate the interaction between the formed ultrathin hydroxide nanosheets and the –NH_2 groups. As shown in Fig. 4B, the intensity of the peak located at 3702 cm^{-1}, which can be ascribed to the O–H stretching mode of the free Mg–OH groups, presents a gradual increase during the first 2500 seconds, indicating the continuous formation and growth of the $Mg(OH)_2/Mg_2(OH)_3Cl$ nanomaterials during this period. Meanwhile, during the first 2500 seconds, the feature at 1625 cm^{-1} (Fig. 4C) corresponding to the –NH_2 scissoring vibration shows a shape change and a red-shift of 1603 cm^{-1}, while there is no obvious signal change for the CN stretch, CH bend and C═O stretch, suggesting the possible interaction between the –NH_2 groups and the hydroxyl layers of hydroxide. To gain further insights into the role of –NH_2 groups at a molecular level, ^{13}C NMR spectroscopy was applied to investigate six different samples. As shown in Fig. 4D, the spectra of pure water after introducing NH_3 and aqueous solution containing $MgCl_2$ after introducing NH_3 show no obvious peak belonging to the resonance of the carbon atoms, suggesting the absence of carbon. In the spectra of pure formamide aqueous solution, formamide aqueous solution containing $MgCl_2$, formamide aqueous solution after introducing NH_3 without $MgCl_2$ and formamide aqueous solution containing $MgCl_2$ after introducing NH_3, an obvious peak at 168.1 ppm can be seen, which is ascribed to the resonance of the carbon atoms from formamide. Note that one additional peak located at 172 ppm (grey arrow) is only detected in the spectrum of formamide aqueous solution containing $MgCl_2$ after introducing NH_3. The emergence of this new peak indicates the change of the atomic environment of some carbon atoms, which is probably caused by the interaction between the –NH_2 groups connecting with the carbon atoms and the hydroxyl layers of hydroxide. The new peak is absent in the spectrum of formamide aqueous solution after introducing NH_3 without $MgCl_2$, suggesting the unchanged atomic environment of the carbon atoms for such a reaction system, which supports our idea that the NH_2– groups connecting with the carbon atoms interact with the hydroxyl layers of

hydroxide instead of the free hydroxide ions in aqueous solution. Based on the aforesaid analysis, although formamide may serve multiple functions in inhibiting the growth of nanosheets along the *z*-direction, we infer that, except for the unusually high dielectric constant of formamide and interactions between the carbonyl groups of formamide and the hydroxyl layers, the $-NH_2$ groups of formamide play a key role during this process. These findings can advance our understanding of the formation mechanism of ultrathin nanomaterials obtained from the bottom-up fabrication route using formamide as the layer growth inhibitor, and such a perspective could guide us to select the suitable layer growth inhibitor for the future preparation of ultrathin 2D nanomaterials.

Conclusions

In summary, this study has proposed a general and facile strategy to prepare ultrathin 2D metal oxide and hydroxide nanosheets at room temperature by using a wet-chemical precipitation method, which has been successfully utilized to synthesize $Co_3O_4/Co(OH)_2$, γ-Fe_2O_3, Mn_3O_4, ZnO, $Cu(OH)_2{\cdot}H_2O$ and $Mg(OH)_2/Mg_2(OH)_3Cl$ nanosheets. The $-NH_2$ groups of formamide molecules play a key role in further decreasing the thickness of the nanosheets by inhibiting the growth of the nanosheets along its *z*-direction, which is supported by the results of FTIR spectroscopy and NMR spectroscopy. These findings can not only broaden the fundamental understanding of the formation mechanism but also provide a guiding principle for selecting a suitable layer growth inhibitor. Since the growth mechanism is mainly dependent on the layered structure character, this approach should be versatile and transferable to more materials with a similar structure, opening up new opportunities for an easy, general and low-cost synthesis of ultrathin 2D metal oxide and hydroxide nanosheets.

Conflicts of interest

The authors declare no competing financial interest.

Acknowledgements

This research was funded by the Deutsche Forschungsgemeinschaft DFG within the framework of the collaborative research center SFB-1214 (Project B1) and the Sino-German Center for Research Promotion (Grants GZ 1351 and CO 194/19-1). Z. C. thanks the Chinese Scholarship Council for a stipend. The authors thank the Particle Analysis Center of SFB1214 at the University of Konstanz for the measurements.

Notes and references

1 X. Xiao, H. Song, S. Lin, Y. Zhou, X. Zhan, Z. Hu, Q. Zhang, J. Sun, B. Yang, T. Li, L. Jiao, J. Zhou, J. Tang and Y. Gogotsi, *Nat. Commun.*, 2016, **7**, 11296.
2 A. Zavabeti, J. Z. Ou, B. J. Carey, N. Syed, R. Orrell-Trigg, E. L. H. Mayes, C. L. Xu, O. Kavehei, A. P. O'Mullane, R. B. Kaner, K. Kalantar-Zadeh and T. Daeneke, *Science*, 2017, **358**, 332–335.
3 W. Sun, X. Rui, J. Zhu, L. Yu, Y. Zhang, Z. Xu, S. Madhavi and Q. Yan, *J. Power Sources*, 2015, **274**, 755–761.
4 P. Zhang, L.-X. Zhang, H. Xu, Y. Xing, J.-J. Chen and L.-J. Bie, *Rare Met.*, 2021, **40**, 1614–1621.
5 J. E. ten Elshof, H. Yuan and P. G. Rodriguez, *Adv. Energy Mater.*, 2016, **6**, 1600355.
6 H. Fan, X. Huang, L. Shang, Y. Cao, Y. Zhao, L. Z. Wu, C. H. Tung, Y. Yin and T. Zhang, *Angew. Chem., Int. Ed.*, 2016, **55**, 2167–2170.
7 X. Mei, S. Xu, T. Hu, L. Peng, R. Gao, R. Liang, M. Wei, D. G. Evans and X. Duan, *Nano Res.*, 2018, **11**, 195–205.
8 Y. Du, Z. Yin, J. Zhu, X. Huang, X.-J. Wu, Z. Zeng, Q. Yan and H. Zhang, *Nat. Commun.*, 2012, **3**, 1177.
9 T. Heine, *Acc. Chem. Res.*, 2014, **48**, 65–72.
10 M. Naguib, O. Mashtalir, J. Carle, V. Presser, J. Lu, L. Hultman, Y. Gogotsi and M. W. Barsoum, *ACS Nano*, 2012, **6**, 1322–1331.
11 C. Xu, L. Wang, Z. Liu, L. Chen, J. Guo, N. Kang, X.-L. Ma, H.-M. Cheng and W. Ren, *Nat. Mater.*, 2015, **14**, 1135–1141.
12 H. O. Churchill and P. Jarillo-Herrero, *Nat. Nanotechnol.*, 2014, **9**, 330–331.
13 H. Wang, X. Yang, W. Shao, S. Chen, J. Xie, X. Zhang, J. Wang and Y. Xie, *J. Am. Chem. Soc.*, 2015, **137**, 11376–11382.
14 A. K. Geim, *Science*, 2009, **324**, 1530–1534.
15 X. Huang, X. Qi, F. Boey and H. Zhang, *Chem. Soc. Rev.*, 2012, **41**, 666–686.
16 H. Yin and Z. Tang, *Chem. Soc. Rev.*, 2016, **45**, 4873–4891.
17 R. Gao and D. Yan, *Nano Res.*, 2018, **11**, 1883–1894.
18 B. M. Hunter, J. D. Blakemore, M. Deimund, H. B. Gray, J. R. Winkler and A. M. Müller, *J. Am. Chem. Soc.*, 2014, **136**, 13118–13121.
19 G. Hu, N. Wang, D. O'Hare and J. Davis, *Chem. Commun.*, 2006, 287–289.
20 J. Yu, B. R. Martin, A. Clearfield, Z. Luo and L. Sun, *Nanoscale*, 2015, **7**, 9448–9451.
21 T. Zhan, Y. Zhang, Q. Yang, H. Deng, J. Xu and W. Hou, *Chem. Eng. J.*, 2016, **302**, 459–465.
22 Y. Yan, Q. Liu, J. Wang, J. Wei, Z. Gao, T. Mann, Z. Li, Y. He, M. Zhang and L. Liu, *J. Colloid Interface Sci.*, 2012, **371**, 15–19.
23 Y. Zhu, C. Cao, S. Tao, W. Chu, Z. Wu and Y. Li, *Sci. Rep.*, 2014, **4**, 5787.
24 M. B. Ghasemian, M. Mayyas, S. A. Idrus-Saidi, M. A. Jamal, J. Yang, S. S. Mofarah, E. Adabifiroozjaei, J. Tang, N. Syed and A. P. O'Mullane, *Adv. Funct. Mater.*, 2019, **29**, 1901649.
25 A. Zavabeti, B. Y. Zhang, I. A. de Castro, J. Z. Ou, B. J. Carey, M. Mohiuddin, R. Datta, C. Xu, A. P. Mouritz and C. F. McConville, *Adv. Funct. Mater.*, 2018, **28**, 1804057.
26 R. Subbaraman, D. Tripkovic, D. Strmcnik, K.-C. Chang, M. Uchimura, A. P. Paulikas, V. Stamenkovic and N. M. Markovic, *Science*, 2011, **334**, 1256–1260.

27 J. Yu, J. Liu, A. Clearfield, J. E. Sims, M. T. Speiegle, S. L. Suib and L. Sun, *Inorg. Chem.*, 2016, **55**, 12036–12041.
28 Z.-P. Sun, L. Liu, L. Zhang and D.-Z. Jia, *Nanotechnology*, 2006, **17**, 2266–2270.
29 E. Darezereshki, *Mater. Lett.*, 2010, **64**, 1471–1472.
30 Y. Oaki and H. Imai, *Angew. Chem., Int. Ed.*, 2007, **46**, 4951–4955.
31 D. Zou, C. Xu, H. Luo, L. Wang and T. Ying, *Mater. Lett.*, 2008, **62**, 1976–1978.
32 X. Li, Y. Fang, X. Lin, M. Tian, X. An, Y. Fu, R. Li, J. Jin and J. Ma, *J. Mater. Chem. A*, 2015, **3**, 17392–17402.
33 J.-X. Feng, S.-H. Ye, X.-F. Lu, Y.-X. Tong and G.-R. Li, *ACS Appl. Mater. Interfaces*, 2015, **7**, 11444–11451.
34 X. Wu, Z. Han, X. Zheng, S. Yao, X. Yang and T. Zhai, *Nano Energy*, 2017, **31**, 410–417.
35 J. Zhang, T. Yao, H. Zhang, X. Zhang and J. Wu, *Nanoscale*, 2016, **8**, 18693–18702.
36 J. Duan, S. Chen, S. Dai and S. Z. Qiao, *Adv. Funct. Mater.*, 2014, **24**, 2072–2078.
37 X. Liu, J. Zhang, L. Wang, T. Yang, X. Guo, S. Wu and S. Wang, *J. Mater. Chem.*, 2011, **21**, 349–356.
38 A. P. LaGrow, L. Sinatra, A. Elshewy, K.-W. Huang, K. Katsiev, A. R. Kirmani, A. Amassian, D. H. Anjum and O. M. Bakr, *J. Phys. Chem. C*, 2014, **118**, 19374–19379.
39 F. Zhang, C. Zhang, R. Zeng, L. Song, L. Guo and X. Huang, *Metals*, 2016, **6**, 85.